Pattern formation in directional solidification under shear flow. II. Morphologies and their characterization

Yannick Marietti,[1] Jean-Marc Debierre,[1] Thomas M. Bock,[2] and Klaus Kassner[3,*]
[1]*Laboratoire Matériaux et Microélectronique de Provence, Case 151, Faculté des Sciences de St. Jérôme, 13397 Marseille Cédex 20, France*
[2]*Institut für Experimentalphysik V, Universität Bayreuth, D-95440 Bayreuth, Germany*
[3]*Institut für Theoretische Physik, Otto-von-Guericke-Universität Magdeburg, Postfach 4120, D-39016 Magdeburg, Germany*
(Received 12 December 2000; published 14 May 2001)

In the preceding paper, we have established an interface equation for directional solidification under the influence of a shear flow parallel to the interface. This equation is asymptotically valid near the absolute stability limit. The flow, described by a nonlocal term, induces a lateral drift of the whole pattern due to its symmetry-breaking properties. We find that at not-too-large flow strengths, the transcritical nature of the transition to hexagonal patterns shows up via a hexagonal modulation of the stripe pattern even when the linear instability threshold of the flowless case has not yet been attained. When the flow term is large, the linear description of the drift velocity breaks down and transitions to flow-dominated morphologies take place. The competition between flow-induced and diffusion-induced patterns (controlled by the temperature gradient) leads to new phenomena such as the transition to a different lattice structure in an array of hexagonal cells. Several methods to characterize the morphologies and their transitions are investigated and compared. In particular, we consider two different ways of defining topological defects useful in the description of patterns and we discuss how they are related to each other.

DOI: 10.1103/PhysRevE.63.066302 PACS number(s): 47.54.+r, 05.70.Np, 81.30.Fb, 64.70.Md

I. INTRODUCTION

In the companion of this article [1], henceforth referred to as I, a discussion of the experiment of directional solidification was given, emphasizing its importance as a tool both for applied and fundamental science. Therefore, we can be brief here in recalling only some of the more noteworthy features.

Concerning pattern formation, directional solidification gives the opportunity mainly to study structures arising from the Mullins-Sekerka (MS) instability [2]. While there are patterns such as lamellar eutectics [3] that are grown in directional solidification and the primary structure of which is not due to this instability, diffusion-induced instabilities do play a major role in eutectic structures as well [4].

In practical applications of crystal growth, convection is a transport mechanism of utmost importance. Hence it seems appropriate to try and capture how it affects growth patterns and length scales, even though one may be able to understand basic patterns and dynamical aspects (dendrites, cells, chaotic behavior) without it and to perform experiments in which it is largely suppressed. Moreover, the possibility of convection-dominated patterns cannot be discarded.

The purpose of the work presented in I and in this article is to demonstrate, for a very simple forced flow, an instability mechanism and its influence on patterns in *three-dimensional* fast directional solidification. In particular, the interaction of the flow-induced instability with the Mullins-Sekerka instability will be a focus of interest here.

An important simplification, rendering possible the study of three-dimensional growth for several hundred solidification cells was the reduction of the full set of model equations to an equation for the interface alone. This motivates the consideration of rapid solidification, where a strongly nonlinear equation of this type can be derived [5,6]. It also restricts the possible flow patterns to simple ones.

It has now become of paramount importance to consider three-dimensional directional growth theoretically, due to the availability of new experimental approaches that allow the *in situ* observation of three-dimensional growth morphologies [7,8]. In these systems, convection turns out to be a nonnegligible effect.

The article is organized as follows. In Sec. II, we recapitulate the basic equation of motion and the definition of the parameters arising therein. Section III describes our methods of pattern analysis by a variety of statistical and topological means and gives its applications to a number of simulation results. Conclusions regarding flow effects and the characterization of morphologies are summarized in Sec. IV.

II. MODEL EQUATION

To make this presentation self-contained we repeat the asymptotic interface equation from I that was used in all the simulations to be discussed:

$$\begin{aligned}\zeta_{tt}-\left(2+\frac{1}{k}+\nu\right)\nabla^2\zeta_t+\left(1+\frac{1}{k}+\nu^2\right)\nabla^4\zeta \\ +8k\nabla^2\zeta+8k\overline{G}\zeta-f\frac{\partial}{\partial x}\mathcal{L}[\zeta] \\ =2\zeta_t\nabla^2\zeta+2(|\nabla\zeta|^2)_t-2\nabla^2(|\nabla\zeta|^2)-2\nu(\nabla\zeta)\nabla(\nabla^2\zeta) \\ -\frac{2}{k}\nabla\{(\nabla\zeta)\nabla^2\zeta\}-2\nabla\{(\nabla\zeta)|\nabla\zeta|^2\}. \qquad (1)\end{aligned}$$

*Email address: Klaus.Kassner@Physik.Uni-Magdeburg.de

 ©2001 The American Physical Society

In this equation, all parameters are already nondimensional. Positions and times are measured in units of a (rescaled) diffusion length and time, respectively. The scalings have been explained in detail in I. $\nabla=(\partial_x,\partial_y)$ is the two-dimensional gradient operator, $\zeta(x,y,t)$ the position of the liquid-solid interface. The temperature gradient is oriented along the z axis, the direction of the flow is determined by the directional derivative of the nonlocal term $\mathcal{L}[\zeta]$, i.e., here it is parallel to the x axis. $\mathcal{L}[\zeta]$ is defined via its Fourier transform

$$\mathcal{F}[\mathcal{L}[\zeta]](\mathbf{p})=|\mathbf{p}|\mathcal{F}[\zeta](\mathbf{p}), \tag{2}$$

where $\mathbf{p}$ is the wave vector in Fourier space.

The nondimensional parameters of the equation are the segregation coefficient k, the ratio $\nu=D_s/D$ of the diffusion coefficients for impurities in the solid and the liquid, the nondimensional temperature gradient $\overline{G}$, and the strength f of the flow. For completeness, we also recapitulate the definition of $\overline{G}$ in terms of physical parameters:

$$\overline{G}=\frac{8D^3L^2m\Delta c}{\gamma^2T_m^2}\frac{G}{V(V_a-V)^2}. \tag{3}$$

Herein, L is the latent heat per unit volume of the transition, m the absolute value of the slope of the liquidus line, Δc the miscibility gap, γ the (isotropic) surface energy. The velocity V_a is given by $V_a=mL\Delta cD/\gamma T_m k$ and corresponds to the absolute stability limit. G is the temperature gradient and V the pulling velocity. In terms of dimensional quantities, the flow strength f reads

$$f=\frac{8V_\infty}{\epsilon VS}, \tag{4}$$

where V_∞ is the speed of the flow far from the interface and $S=\nu_k/D$ is the Schmidt number (ν_k being the kinematic viscosity of the liquid). ϵ describes the distance from absolute stability, $\epsilon=1/2k-\gamma T_mV/2mL\Delta cD$.

To further reduce the parameter space to be explored, we set $\nu=1$ and $k=1$, choices that have been justified in I.

III. GENERAL FEATURES OF THE MORPHOLOGY DIAGRAM

A. Morphology characterization

How to characterize morphologies that can be classified as cellular arrays with a varying degree of disorder has been discussed at length in [9]. Since Fourier transforms and correlation functions are not very good at distinguishing disordered patterns with similar length scales, different tools were employed, based on the analysis of how contour levels of the interface divide the plane into regions. All interface points above a level z_0 belong to one area, called white, all those below to another, called black. For a sufficiently large z_0, the white area consists of separate clusters, as can be gathered from the example given in Fig. 1. A way to describe the interface using a meaningfully reduced amount of information is the *cluster number function* $N_w(z)$ counting the white clusters.

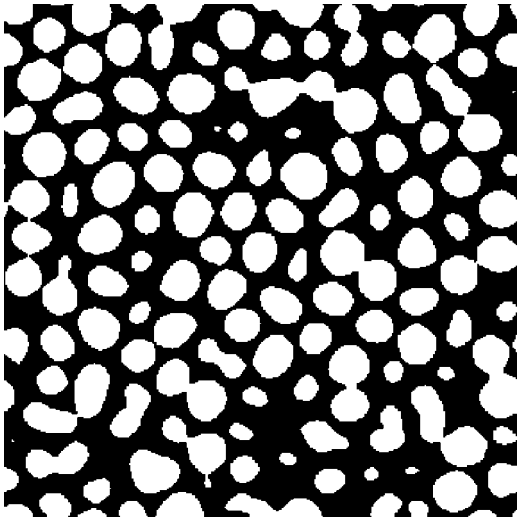

FIG. 1. Division of the plane into black and white regions by level contours. The whole interface (obtained for $\overline{G}=0.25$, no flow, at $t=50$, after random initialization) was divided into 254 equidistant levels. Cutting at level 145 yields the shown image. At a lower level, more white regions would be connected, their total area would be larger, and, if the level were taken sufficiently low, there would be several disjoint black regions.

Once clusters corresponding to solidification cells are defined (by an appropriate choice $z=z_0$), disorder may be characterized via construction of the minimum spanning tree on the set of centers of mass of the clusters [10] or by defect counting in the Voronoi graph of these centers, where a defect is any cell with an edge number different from six.

Both the minimum spanning tree and defects whose definition is based on the Voronoi construction become pretty much useless when the structure changes from cellular to striped, a situation demonstrated in I. Cluster counting remains informative, however, as will be clarified by our discussion of the Euler characteristic below.

It has been proposed [11] that morphological measures such as the area a of the white regions, their boundary length s and their Euler characteristic χ would be useful in describing transitions between different morphologies such as hexagonal and striped ones. The Euler characteristic is, up to a constant factor, the total integral of the curvature of the boundary between black and white domains, and it can be shown to be equal to the difference between the numbers of connected white and black regions (not counting the all-encompassing outermost region). In other words, if we define, besides our cluster number function for white regions $N_w(z)$, the corresponding function $N_b(z)$ for black ones, then the Euler characteristic is given by

$$\chi(z)=N_w(z)-N_b(z)(\pm 1), \tag{5}$$

where the added or subtracted 1 accounts for a black or white background [13]. As soon as we have just white cells on a

connected black background, the Euler characteristic becomes equal to the cluster number function $N_w(z)$.

It can be proven that the Minkowski functionals *a*, *s*, and χ form a complete set of additive, motion invariant, conditionally continuous functions in two dimensions [12], i.e., any functional of sets in the plane satisfying these three conditions can be expressed as a linear combination of the three Minkowski functionals. Additivity means that the functional of the union of two sets *A*, *B* is given by

$$M(A\cup B)=M(A)+M(B)-M(A\cap B), \tag{6}$$

and motion invariance implies invariance under translations and rotations.

We shall see that in particular the Euler characteristics, measuring the connectivity of a pattern, is a very good means indeed to distinguish between flow-induced and diffusion-dominated patterns. Nevertheless, the extraction of order parameters from these measures is not as straightforward as suggested in [11].

A tool of characterization that works for both hexagonal and oriented striped patterns, as long as the defect density is not too high, *and* yields the order parameter(s) corresponding to an appropriate amplitude equation of known general form, is *complex demodulation*.

The principle is simple. Assume we have a pattern of the form

$$\zeta(x,y)=A(x,y)e^{ikx}+\text{c.c.}, \tag{7}$$

where *A* is a slowly varying complex amplitude. Using the convolution theorem, we see that the Fourier transform of this contains a term of the form

$$\int \mathcal{F}[A](\mathbf{p}-\mathbf{p}')\,\delta(\mathbf{p}'-k\mathbf{e}_x)d^2p'=\mathcal{F}[A](\mathbf{p}-k\mathbf{e}_x), \tag{8}$$

i.e., the spectral intensity corresponding to the amplitude *A* is centered about $\mathbf{p}=k\mathbf{e}_x$. There will be a second peak at $-k\mathbf{e}_x$, stemming from the complex conjugate. Throwing away this part, i.e., the half of the spectrum in the negative k_x half plane, and shifting the remaining pattern in Fourier space by $-k\mathbf{e}_x$ one moves the peak of the transform to the origin of the $\mathbf{p}$ plane. All wave numbers with modulus larger than a few times *k* are then filtered out. Transforming back to position space one obtains the complex amplitude $A(x,y)$, which may directly serve as an (albeit space dependent) order parameter of the pattern. For a more elaborate description of the procedure as applied to experimental patterns, see [14].

If the pattern is basically hexagonal, this procedure should be analogously performed three times (once for each of the three different orientations of the basic wave vector about which the spectral intensity is centered) to obtain the complex amplitudes of the three stripe systems from which a hexagonal pattern can be constructed by superposition. The order parameter of the pattern would then be a complex-valued three-dimensional vector (A_1,A_2,A_3), describing all the stripe patterns.

Defects are positions where the complex amplitude becomes zero, as the phase gets undefined there and can jump. In the case of hexagons, we will consider each defect in an underlying stripe system a defect of the whole pattern. Then defects can be detected by finding the places where the *product* $A_1A_2A_3$ becomes zero. We will demonstrate the applicability of the method here but not try to develop the detailed equations for the complex amplitude.

B. Generic patterns

We organize our discussion of systematic features of numerically simulated patterns by considering the different morphologies that evolve at fixed temperature gradient as the flow strength is increased. Next we decrease the temperature gradient, moving farther into the unstable region of parameter space and again study the changes on increase of the flow. The numerical procedure has been described in I. Each run is initialized with a random interface at zero velocity ($\zeta_t=0$), many of them with the same random seed to allow for a more straightforward comparison. The seed was varied as a countercheck of the genericity of arising patterns.

Running the system for 2000 (rescaled) diffusion times was largely sufficient to reach a (statistically) invariant state when hexagonal patterns appeared. Stripe structures usually reached a typical state much faster. In this article, we restrict ourselves essentially to the part of parameter space, in which patterns keep a certain degree of order. Outside this region, i.e., for even smaller temperature gradients and larger flows, the typical behavior is complex in time and mostly weakly turbulent. We have not yet been able to simulate large enough systems for a sufficiently long time to give a more thorough analysis of these spatiotemporal patterns.

At $\bar{G}=0.7$, the minimum flow strength to see any patterns at all is $|f|=8/\sqrt{15}\approx 2.066$. We start with $f=4.0$ and consider increasing values of *f*. (Negative *f* values give equivalent patterns with opposite drift velocity.)

A typical state for $f=4.0$ at an intermediate time ($t=150$) has been given in Fig. 4 of I. Including some additional information in the picture, we display this pattern once again in Fig. 2.

Defects terminate a bright stripe (a crest) and start off a dark one (a trough) or vice versa. There are two kinds of defects of opposite topological charge, those that constitute the upper end of a dark stripe and those that constitute the lower one; of course, these descriptions could also be based on the complementary behavior of bright stripes. Note that due to the periodic boundary conditions, defects always occur in pairs. In a real system, a single defect might exist.

In the example, all defect pairs except three have already gone. Elimination of the remaining defects takes rather long, with a reduction to two pairs occurring between $t=150.0$ and $t=200.0$, one more pair disappearing between $t=900.0$ and $t=1000.0$, and the final pair still existing at $t=9200$. Since the last two defects travel through the system as a closely bound pair (see Fig. 6), it is quite possible that they will never recombine. The longer survival of defects with decreasing defect number is understandable from the fact that their elimination serves the purpose of wavelength adapta-

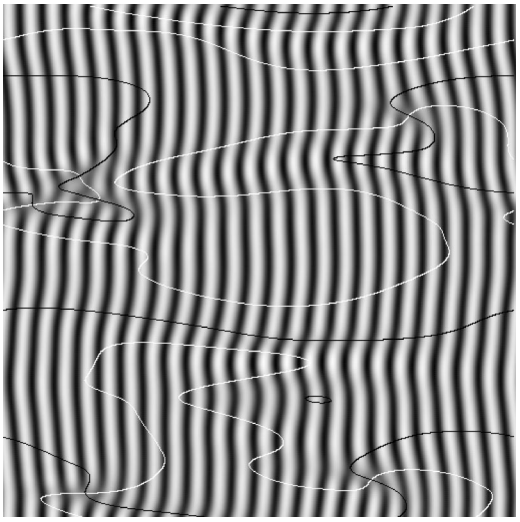

FIG. 2. Pattern of Fig. 4 of I with superimposed curves of zero real and imaginary parts of the amplitude.

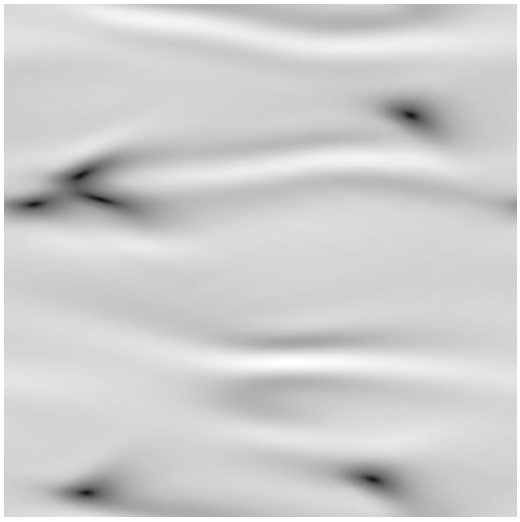

FIG. 4. Absolute value of the complex amplitude of the pattern of Fig. 2.

tion and that the wavelength is already close to a preferred value when only a few defects remain.

A precise definition of a defect, not relying on purely visual inspection of the pattern, is based on the complex demodulation procedure described above. Defects are locations of vanishing complex amplitude, which may be obtained by tracing the curves of vanishing real and imaginary parts, which are shown in Fig. 2, together with the pattern.

Black curves correspond to vanishing imaginary part (i.e., a purely real amplitude), white ones to vanishing real part (i.e., a purely imaginary amplitude). Intersection points give defect positions and it is evident that they roughly coincide with ending stripes.

The topological charge of a defect may be determined from the sense of rotation about it that leads to an increasing phase. Figure 3 shows a reduced phase plot for the structure of Fig. 2. The reduction consists in restricting the picture to four gray scales with dark gray corresponding to phases between 0 and $\pi/2$, gray to phases between $\pi/2$ and π, light gray to phases between π and $3\pi/2$, and finally white to phase angles from $3\pi/2$ to 2π.

We also give the modulus of the complex amplitude, in Fig. 4; bright regions mean large amplitude, dark ones small amplitude, and defects are ''black holes'' in this representation.

An earlier structure is shown in Fig. 5. It still contains many defects producing horizontal bands interrupting the continuity of the vertical stripes. These are sequences of defects where an array of bright stripes is shifted by half a wavelength with respect to their counterparts on the other side of the defects. Most of the defects in such a band disappear rapidly by an adjustment of the lateral positions of the stripes.

The dynamics of a single defect is easy to describe. The whole pattern moves to the left (to the side where the flow comes from), but the end of a stripe moves more slowly, so it curls, moving sideways relative to the stripe pattern until it

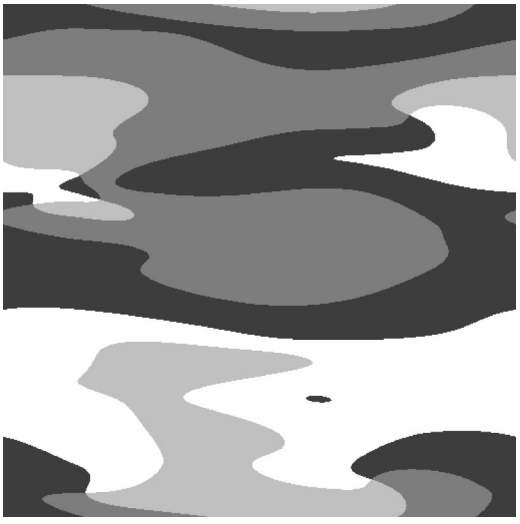

FIG. 3. Phase plot for the pattern of Fig. 2.

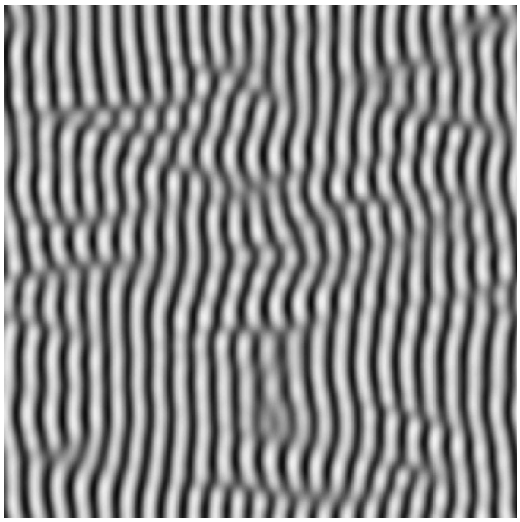

FIG. 5. Pattern of the system of Fig. 2 at an earlier time ($t = 50.0$).

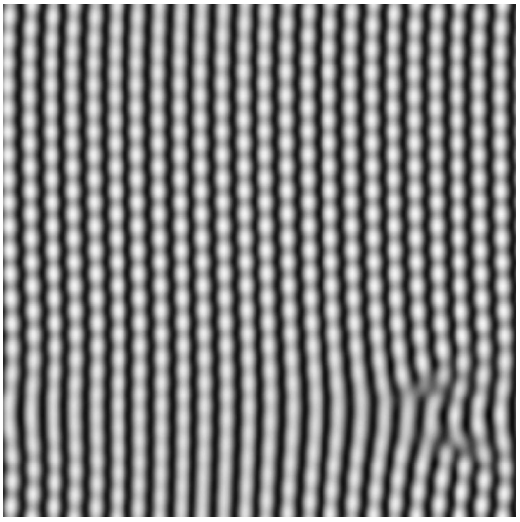

FIG. 6. Pattern of the system of Fig. 2 at a very late time ($t = 7000.0$). Stripes have become modulated to produce a structure with a strongly hexagonal aspect.

hits the neighboring stripe. It merges with the latter, a bright stripe end thus being eliminated creating a fork-shaped bright structure. This structure breaks up on the right side, with a bright stripe end reappearing. In consequence, the stripe end has moved to the right by one wavelength and as it turns out, this movement is fast enough to keep the defect almost in place, i.e., to render its motion much slower than that of the pattern. In terms of amplitude equations, the lateral motion of the modulated underlying structure is governed by the flow, whereas the slowly varying amplitude is almost decoupled from it.

Defects of opposite topological charge annihilate each other when they meet, which suggests the final state to be a completely ordered array of stripes, a question to which we will return shortly. Mutual annihilation requires a certain amount of up-down (climbing) motion of defects besides the described left-right (gliding) motion. Such a motion is explicable in terms of an attractive force between oppositely charged defects. A slightly more detailed description of the dynamics of pairs of defects can be found in [15].

In electroconvection experiments, certain liquid crystal systems develop morphologically very similar patterns and display a comparable defect dynamics, when they have traveling wave states. Of course, in these systems the mere appearance of traveling waves is a much less trivial matter than in ours — the standard model of electroconvection of nematics was not capable to predict them. They were found experimentally first [16–18] and the defect dynamics in these systems was linked to the appearance of turbulent states [19]. To explain them [20], the theory had to be generalized to the weak-electrolyte model. In our system, the prediction of traveling waves can be almost made after a first glance at the equation of motion (1), in which the left-right symmetry is already broken, whereas in the electroconvection system we have *spontaneous* symmetry breaking. Moreover, in those systems the case of nontraveling patterns also appears, which may contain defects, too, with a somewhat different defect dynamics.

The idea conveyed so far, that the final pattern will consist of stripes as long as $\overline{G}$ stays above the threshold value for the instability in the absence of flow, cannot be upheld. In fact, after $t = 1400.0$, the stripes of the pattern of Fig. 2 start to get modulated in the direction perpendicular to the flow and almost dissolve into cells. Figure 6 shows the pattern at $t = 7000.0$. The structure is intermediate between striped and hexagonal. Its topology is essentially that of the hexagonal lattice but the hexagonal symmetry is broken due to the nonequivalence of the grooves between the cells in different directions.

The reason for the appearance of this pattern is the *transcritical* nature of the bifurcation to hexagons, signifying that hexagons can exist already *below* the bifurcation point, if the amplitude of the pattern becomes large enough (they sit on the subcritical branch of the transcritical bifurcation). So the scenario is that the stripe structure serves to destabilize the planar interface and once it has grown enough, it becomes unstable to modulations due to the presence of a hexagonal branch at finite amplitude. The unmodulated stripes therefore are but a long-living transient at $f = 4.0$, which is not too far above the critical flow value ($f = 2.066$).

With increasing flow strength, the unmodulated stripe pattern does become stable, however. For $f = 6.0$, we have carried the simulation beyond $t = 8000.0$ as well and the stripes keep their homogeneity. The defect dynamics is not very different from the case $f = 4.0$; by $t = 200.0$, the number of defect pairs has reduced to three, by $t = 400.0$, to two, by $t = 500.0$, to one, and there it stays up to $t = 10\,000.0$, with the defects approaching each other but not annihilating.

As the flow is increased further, the stripe patterns first seem to become more pronounced to reduce their defect numbers in a shorter time. At a flow of 9.0, defects become more frequent again and for larger flows the pattern turns wavy and more disordered.

Another interesting case is $\overline{G} = 0.6$, where we can compare with extensive simulations from [9]. The most striking effect of a small flow is that it seems to increase the ordering tendency of the hexagonal basic structure. For example, counting the defect cells (i.e., cells with a number of neighbors different from 6, where neighbor counting is based on the Voronoi construction [9]) at time $t = 2000$ for systems of size 128.0×128.0, we find the following table:

f	No. of defects	Total no. of cells	% defects
0.0	44	472	9.32
1.0	16	475	3.37
2.0	39	473	8.25
3.0	0	472	0.00
4.0	0	486	0.00

The pattern at $f = 2.0$ (see Fig. 5 of I) has more defects than the one at $f = 1.0$ but it still looks more ordered than the latter (not shown), its defects being due to the presence of two domain walls, whereas in the case of $f = 1.0$ they are scattered all over the system. For the flows 3.0 and 4.0, the system is completely ordered. In the former case, the pattern is a perfect hexagonal structure, which we will not show

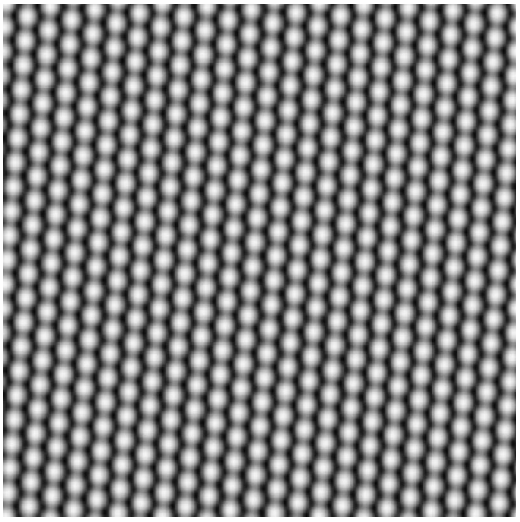

FIG. 7. Pattern at $t=2000.0$, $\overline{G}=0.6$, and $f=4.0$. System size: 128.0×128.0.

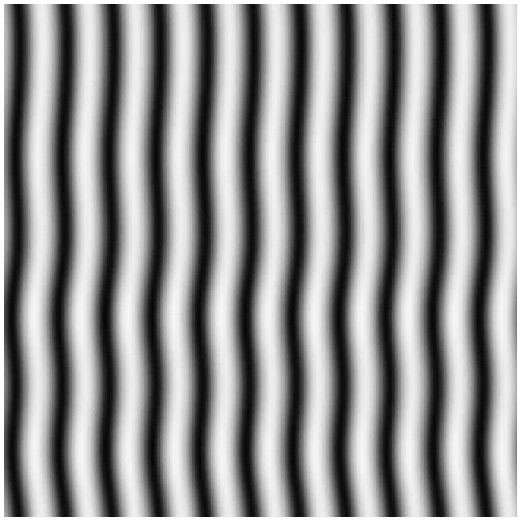

FIG. 8. Pattern at $t=2101.0$, $\overline{G}=0.6$, and $f=5.0$. System size: 64.0×64.0.

here, since everybody can imagine what it looks like. We will, however, give the second pattern (Fig. 7), because it displays an interesting phenomenon, related to the fact that the total number of cells suddenly becomes distinctly larger at $f=4.0$.

The striking feature to be noted here is that the pattern undergoes a transition to a different ''crystal structure,'' losing its hexagonal symmetry and becoming rhombic. Single cells still keep their hexagonal shape, but grooves between cells become deeper in the transverse direction than parallel to the flow. This pattern is similar to the modulated stripes discussed before, however, here the cell aspect is much more pronounced. Both patterns appear by similar dynamic processes: Up to $t=500.0$, the system shown in Fig. 7 contains stripes that start to get modulated, while there is still an appreciable number of defects. At $t=675.0$, more than half the system consists of cells that invade the remaining stripes. That is, cells appear earlier here than in the case of Fig. 2 and they develop fully, rendering the final pattern ''cellular'' rather than ''striped.''

A more dramatic transition is imminent: at $f=5.0$, the hexagonal structure gets lost and up to $f=7.0$, we see only ordered stripe structures, an example of which is shown in Fig. 8.

The stripe pattern is defect free already at $t=110.0$ and all that happens up to the time displayed is a reduction of the waviness of the structure. For $f=7.0$, the stripes are completely straight at $t=2000.0$. There is not much change as f is increased to 8.0, but a new structure arises at $f=9.0$. This can be anticipated from a comparison of the drift velocity as computed from linear stability analysis with that measured in the simulation, given in Fig. 9.

Whereas up to $f=8.0$ the agreement between the analytical expression for the velocity and the simulation is almost perfect, strong deviations are obtained for $f=9.0$ and $f=11.0$. At $f=8.0$, the final pattern still consists of perfectly straight stripes, whereas both the structures for $f=9.0$ and $f=11.0$ appear turbulent. We show the case $f=9.0$ in Fig. 10.

We shall now consider the utility of Minkowski functionals in characterizing structures and in particular in distinguishing between different ''phases'' corresponding to distinctly different morphologies. First, it should be noticed how these measures scale with system size. If we simply increase each length by a fixed factor λ, then the area scales as λ^2, the boundary length as λ, and the Euler characteristic remains invariant. However, for patterns with a *well-defined length scale,* increasing the system size means a change in the *number* of substructures, not in the pattern scale. If we double the linear dimension of a system, then the number of cells and hence the Euler characteristic will be multiplied by a factor of four. The same holds for area and boundary length. Therefore, measures that allow to compare systems of different sizes, because they are (apart from random fluctuations) independent of size, are given by the normalized area fraction a/N (area measured in units of the pixel size divided by the number N of pixels), the normalized boundary length s/N, and the normalized Euler characteristic χ/N.

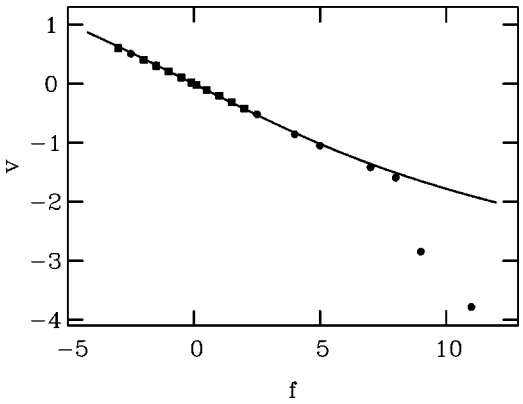

FIG. 9. Comparison of drift velocity as predicted from linear stability analysis (continuous line) with the measured velocity for $\overline{G}=0.6$. Squares are data obtained with the mixed code; circles, with the spectral code.

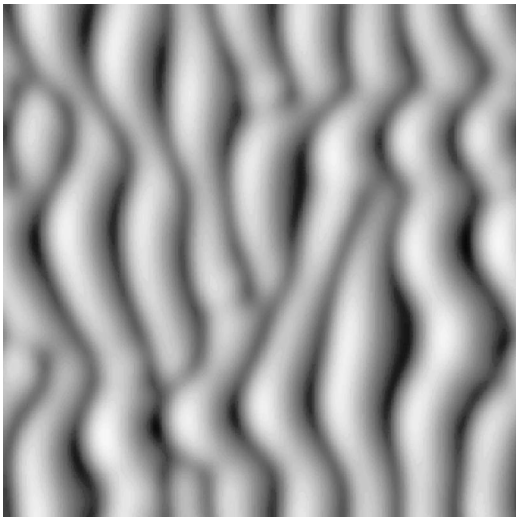

FIG. 10. Pattern at $t=2000$, $\overline{G}=0.6$, and $f=9.0$. System size: 64.0×64.0.

We have verified that for systems with the same parameters but different system sizes (64.0×64.0 and 128.0×128.0, respectively) these morphological measures remain the same, apart from statistical fluctuations.

After dividing the interval between the minimum and the maximum of the interface into 254 equidistant levels, Fig. 11 gives the area fraction of white regions as a function of the level number for several flows. It is quite evident that the behavior of this quantity depends strongly on the flow and thus seems to characterize the corresponding morphologies well. At small flows ($f\leqslant4.0$), i.e., for the hexagonal structures, the area fraction starts with a horizontal tangent and bends down smoothly (thick solid, dashed, and dotted lines), whereas for ordered stripe structures it falls much more abruptly (dash-dotted and thin solid lines); as the stripe structures become turbulent, the white area fraction increases strongly for threshold values below 150 (thin dashed line). Note that even the transition from a lattice of hexagonal symmetry to a rhombic one is visible in the curve for $f=4.0$, which has a second shoulder near level 130. This shoulder is due to the fact that there are minima of two different depths (the grooves between lines of cells and those between cells in a line), which discontinue contributing to the area fraction at different level heights.

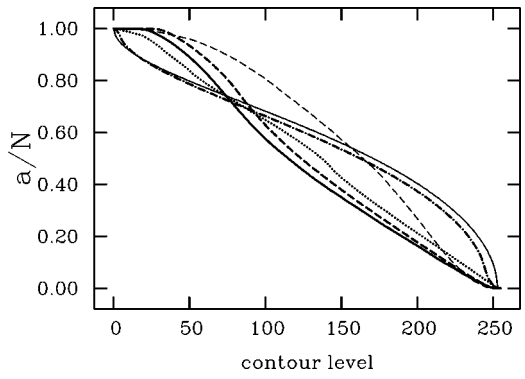

FIG. 11. Area fraction of white region as a function of the chosen value of contour level for a number of different systems with $\overline{G}=0.6$ at a late stage of the evolution. Thick solid line, $f=0.0$; thick dashed line, $f=2.0$; dotted line, $f=4.0$; dash-dotted line, $f=5.0$; thin solid line, $f=7.0$; thin dashed line, $f=9.0$.

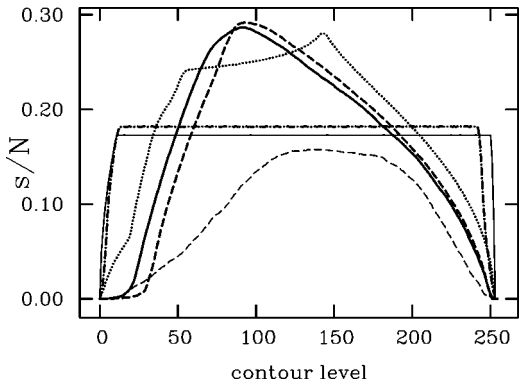

FIG. 12. Boundary length of white region normalized by the total area as a function of the chosen value of contour level for the same systems as in Fig. 11. Thick solid line, $f=0.0$; thick dashed line, $f=2.0$; dotted line, $f=4.0$; dash-dotted line, $f=5.0$; thin solid line, $f=7.0$; thin dashed line, $f=9.0$.

The different behavior of the area fractions of hexagonal and stripe structures can be understood from the fact that for the latter there is an approximate symmetry between protrusions and grooves that makes a/N nearly point symmetric [about the point (127.5,0.5)], whereas for hexagons the up-down symmetry is strongly broken.

Also the second morphological measure, the normalized boundary length, undergoes remarkable changes as a function of structure. In Fig. 12, it is given for the same systems as the area fraction before.

The essentially hexagonal structures show big asymmetric humps, with the transition at $f=4.0$ leading to an exotic-looking combination of a shoulder and a peak. The two regular stripe structures have constant boundary lengths over a wide range of levels; that this range is wider for $f=7.0$ suggests this pattern to be even more ordered than the one at $f=5.0$, a conjecture that will be confirmed by a look at the Euler characteristic. Moreover, the turbulent structure has a broad rounded-off hump because the interface height varies irregularly in space and thus moving the contour level implies its length changing.

Finally, we consider the Euler characteristic (Fig. 13). For a hexagonal structure, it has a pretty distinctive behavior (thick solid and dashed lines): there are approximately twice as many minima as maxima in the structure, which produces twice as many black clusters at low level values than white ones at high values. The hump corresponding to the white clusters is wider than the trough corresponding to the black ones, because the minima are less pronounced than the maxima. The characteristics of these two patterns have rounded shapes, they still contain some disorder, either in the form of defects or by cells varying in height — otherwise the transition from $\chi<0$, i.e., more black than white regions, to $\chi>0$, i.e., more white than black regions, would be a jump discontinuity.

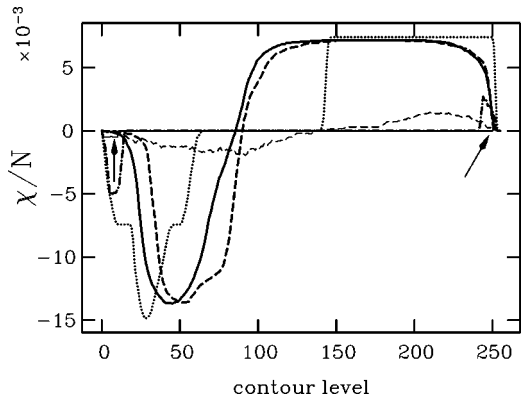

FIG. 13. Euler characteristics normalized by the total area as a function of the chosen value of contour level for the same systems as in Fig. 11. Thick solid line, $f=0.0$; thick dashed line, $f=2.0$; dotted line, $f=4.0$; dash-dotted line, $f=5.0$; thin solid line, $f=7.0$; thin dashed line, $f=9.0$. Since the curve for $f=7.0$ is unconspicuous among the others, two arrows indicate where it is different from zero (between level 1 and 10, where it is negative, and for levels 251 and 252, where it is positive).

That the pattern at $f=4.0$ (dotted line) is topologically distinct from the others is nowhere more conspicuous than in the Euler characteristic. The existence of several plateaus shows the corresponding structure to be very regular— moving a contour level up does not change the number of regions as long as no extrema are crossed; for an irregular structure this must happen continuously, with a regular one, many extrema are crossed at the same time. There is a wide region in which the Euler characteristic is zero. This corresponds to a situation where the cutting level is above the minima of the deep grooves but below those of the smaller grooves between cells ''in a stripe.'' Figure 14 clarifies this point: for levels in this range the white and black clusters are essentially stripes.

The two ordered stripe patterns ($f=5.0$ and $f=7.0$, dash-dotted and thin solid lines) are distinguished by having a very large range of vanishing characteristic — in this range of cutting levels (between 20 and 230) the number of black and white regions (the regions being stripes) is the same — and a small number of components when the Euler characteristic is nonzero. Here we can see that the pattern corresponding to $f=7.0$ is more ordered than that at $f=5.0$, for the absolute value of its Euler characteristic remains much smaller at small levels and at large ones than that of the latter. The number of components never gets larger than the number of stripes for $f=7.0$ but it does for $f=5.0$ (there are on the order of 10 stripes and χ takes on values on the order of 50). This is explicable by the stripes having inhomogeneous heights and depths in the case $f=5.0$, which lead to their separation into elongated ''cells'' when they are cut at an appropriate level, whereas they seem to be pretty homogeneous for $f=7.0$.

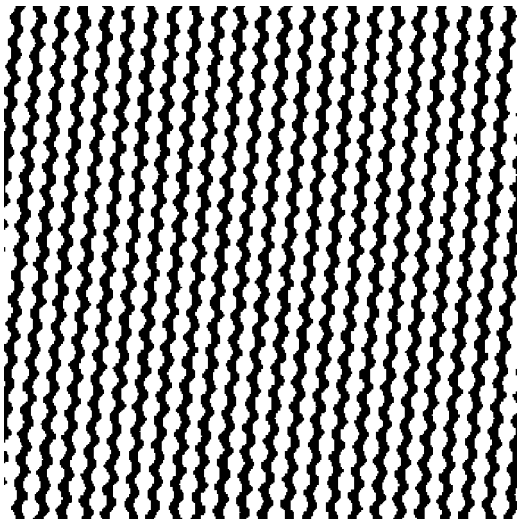

FIG. 14. Black and white regions for the pattern from Fig. 7 at contour level 120, where the Euler characteristics are zero (see Fig. 13).

Finally, the Euler characteristic of the turbulent stripe pattern is broad and roundish, showing that disorder is present, and almost point symmetric, showing that we have stripes rather than hexagons.

From the functional dependencies of the morphological measures presented so far, it should be obvious that they can hardly be fitted to a half-decent degree of accuracy by low-order polynomials. Such a fit was suggested in [11] as a means of extracting a small number of order parameters describing the morphology. More precisely, the suggestion was not to fit the morphological measures themselves but rather the following quantities:

$$p_a(\rho)=\tanh^{-1}\left(\frac{2a}{N}-1\right), \tag{9}$$

$$p_s(\rho)=\frac{s}{a(a/N-1)}, \tag{10}$$

$$p_\chi(\rho)=\frac{\chi}{s}, \tag{11}$$

where ρ was the level value, mapped to the interval $[-1,1]$. With digitized images of structures in chemical reaction systems, these quantities seem to be fitted well by polynomials of at most quadratic order [11]. In our case, this did not work at all; attempts to fit the morphological measures themselves with polynomials gave acceptable results only for the area fraction but even then higher-order polynomials were needed ($\approx$ order 10). That polynomials are not good at describing step functions is well-known. Therefore, our inability to get a good representation of the Minkowski functionals themselves by polynomial fitting may be traced back to the fact that we have structures that are more ordered than the ones seen in the experiments on reaction-diffusion patterns. On the other hand, a fit of the quantities defined in Eqs. (9)–(11) does not work well either, which is not too surprising. $p_a(\rho)$ diverges logarithmically as a/N approaches the values 0 or 1 and $p_s(\rho)$ diverges algebraically ($\propto\sqrt{1/a}$ for small a) at the boundaries of the domain of definition of the functionals. Polynomials are notorious for not dealing too well with singularities either.

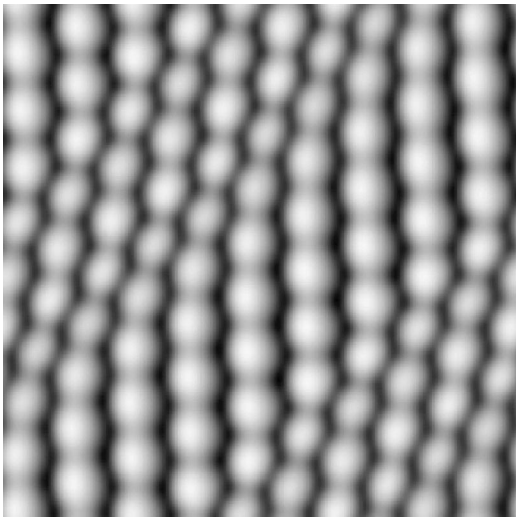

FIG. 15. A structure near the transition from cells to stripes. $\overline{G}=0.4$, $f=7.0$, $t=2000$.

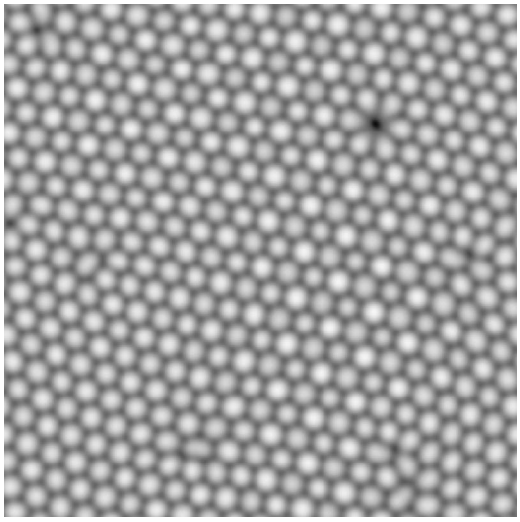

FIG. 16. Pattern at $\overline{G}=0.35$, $f=1.0$, system size 128.0×128.0, $t=2800$.

Thus we are not able to obtain a small number of order parameters from the Minkowski functionals in this simple manner, even though at least the Euler characteristic is definitely well-suited as an order parameter *function* describing transitions between patterns. Integrals of the Minkowski functionals when taken as a function of the level might provide useful practical order parameters; nevertheless, a connection to equations giving their evolution is not straightforward.

After this somewhat lengthy discussion of the case $\overline{G}=0.6$, we can be less detailed about smaller values of $\overline{G}$. For $\overline{G}$ down to 0.4, the scenario is essentially the same, except that defects are more frequent in the hexagonal structures and the transition to stripes takes place at larger values of f only — near $f=7.0$, see Fig. 15. The undulations of the stripes in this figure also suggest that the transition is not stationary as for $\overline{G}=0.6$.

Moreover, there are intermediate structures at relatively large f ($f=6.0$) that display oscillations, comparable with but dynamically more complex than, the $2\pi/3$ oscillations mentioned above. An investigation similar to that of Fig. 9 shows that the difference between the drift velocity from linear stability analysis and that from the numerical simulation appears *earlier*, i.e., at lower f values than for $\overline{G}=0.6$. This should caution against direct use of this deviation as a criterion for a morphology transition. While a transition in general will lead to a deviation from linear theory, the latter may also occur without transition, simply due to the increasing influence of nonlinearities as one moves farther away from the instability threshold.

The new important feature at $\overline{G}=0.35$ is the appearance of $2\pi/3$ oscillations at small values of the flow. An example with perfect topological order has been shown in I (the flow was $f=2.0$). At a smaller flow ($f=1.0$), a less ordered structure turns up, the cells of which do not form a perfect hexagonal lattice. It is shown in Fig. 16. Note that oscillations, inferable from the presence of triangles of brighter cells, are less pronounced for $f=1.0$ than for $f=2.0$ and they do not seem to prevail in the entire area of the pattern.

If there is no flow, the structure is a simple disordered hexagonal array without any sign of spatially correlated oscillations. In small systems, patterns may even become ordered because the dynamics is more violent than at higher $\overline{G}$ and defects less likely to be frozen in. Also, a new type of defect seems to appear more often at low gradients, describable as inverted cells, i.e., cells that bulge downward instead of upward. Examples are to be seen in Figs. 16 and 17.

In the latter figure we give the lines of vanishing real and imaginary parts of the product of the three amplitudes A_1, A_2, A_3 corresponding to the three stripe systems from which the hexagons can be composed. While probably no deeper meaning can be assigned to these lines themselves (since

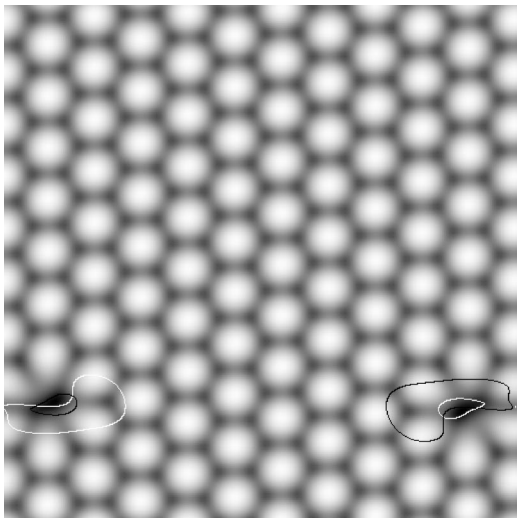

FIG. 17. A frozen hexagonal structure in a small system (64.0×64.0). $\overline{G}=0.35$, $f=0.0$. $t=2000$. Superimposed on the picture are the lines of vanishing real (white) and imaginary (black) parts of the product of the three amplitudes defining the hexagonal structure.

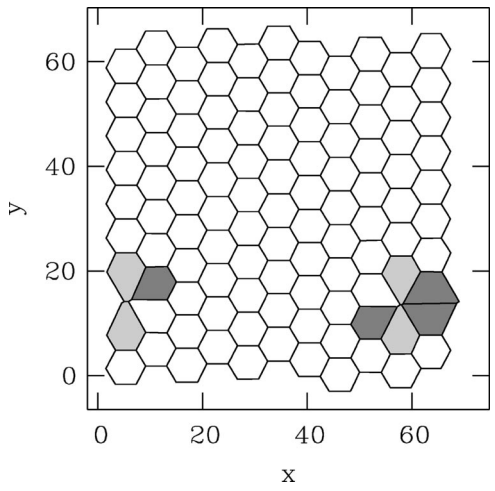

FIG. 18. The Voronoi diagram of the cell structure of Fig. 17.

they describe neither of the underlying stripe systems), their *intersections* are meaningful. They correspond to zeros of the product, hence to zeros of one of the underlying amplitudes at least. By this method we may thus identify all the topological defects, apart from possible (but rare) degeneracies, where we might count a double or triple zero (due to more than one amplitude vanishing simultaneously) as only one defect.

We note that each of the inverted cells corresponds to two (oppositely charged) defects of the underlying stripe systems. One of the stripe structures is defect free, as inspection of the separate amplitudes reveals, whereas the other two have one defect each near the position of the inverted cell. Each of the two stripe systems has two defects of opposite charge (since the total charge must be zero in a periodic system), one at each inverted cell. Therefore, the total number of topological *amplitude defects* is four.

In order to compare this approach with the method of defining defects in a cellular structure via neighborhood relationships [9], we give the corresponding defect picture as obtained from the Voronoi diagram of the cell centers in Fig. 18. The construction of this diagram is described in Sec. III C and, in more detail, in [9].

Defects are cells with a number of edges smaller or larger than six. Since the average number of edges must be equal to six in the plane, the simplest possible defect configuration is the penta-hepta defect, consisting of a pair of cells, one of which is a pentagon, the other a heptagon. As it turns out, most defects occurring at all are pentagons or heptagons. In the figure, pentagons are presented in dark gray, heptagons in light gray, whereas hexagons remain white. Each of the inverted cells corresponds to a pair of penta-hepta defects; due to the periodic boundary conditions, one of the pentagons of the left defect appears near the right boundary. Note also that these are really pentagons although some of them look very much like quadrangles — their fifth edge is just very short.

At this point, it might seem that there is a one-to-one correspondence between the two different kinds of topological defects defined. A zero in a component of the complex amplitude vector appears to be equivalent to a penta-hepta defect. Unfortunately, things are not that simple as we shall see by considering a slightly more complex example, given in Fig. 19.

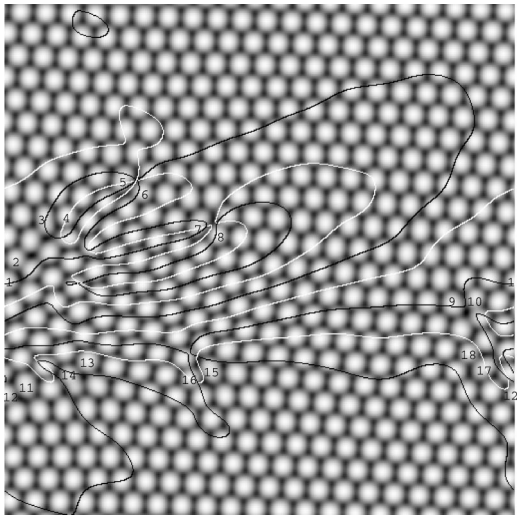

FIG. 19. The other type of defects in hexagonal cellular arrays, demonstrated on a structure with $\overline{G}=0.45$, $f=3.0$, $t=2042$. Again defects as defined via the amplitude can be found as intersections between the lines of vanishing real (white) and imaginary (black) part of the product of amplitudes.

Here we have a larger value of $\overline{G}$ and no inverted cells occur. Instead, defects are of the standard type (bigger or smaller cell surrounded by more or less than six neighbors). The figure also contains the lines whose intersections define amplitude defects.

In the following figure (Fig. 20), the Voronoi graph corresponding to Fig. 19 is given. Defect cells are numbered in order to facilitate comparison between the interface picture and the Voronoi diagram. Heptagons are given odd numbers, pentagons even ones, and there are nine pairs of defects in all.

We note that certain among these pairs, e.g., no. 3 and 4, 5 and 6, 7 and 8, 13 and 14, 15 and 16, are associated with two crossings of contours of zero real and imaginary part,

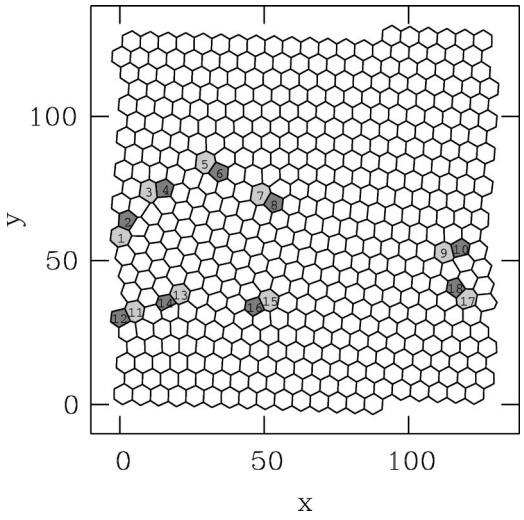

FIG. 20. The Voronoi diagram of the cell structure of Fig. 19.

i.e., they correspond to two amplitude defects as before. For others, such as the pairs 9 and 10, 11 and 12, 17 and 18, there is only one amplitude defect that is nearby and thus easily identifiable with the penta-hepta defect (for the pair 17, 18 even this is doubtful, one might as well associate two line crossings with the pair 11, 12). Finally, the pair 1, 2 is not easily associable with any amplitude defect at all, and there is a ''freely floating'' amplitude defect three cells to its right.

The reason why the correspondence between amplitude and Voronoi defects does not work too well in this case is probably that the basic hexagonal pattern is already too strongly disturbed by the nine penta-hepta defects for the description by three amplitudes to be very meaningful. We do not have just one orientation of the hexagonal lattice but essentially two grains, one of which is encircled by the Voronoi defects, while the other is outside of them (the pairs 9, 10 and 17, 18 close the inner grain at its ''left'' end, due to the periodic boundary conditions). Choosing just three peaks in the Fourier spectrum for complex demodulation, we therefore miss some information and some of the amplitude defects appear shifted relatively far from the cells generating them. That in some cases only one amplitude defect appears for a given penta-hepta pair may be due to the closeness of the next pair and the ensuing interaction of defects. The four pairs that have only a single amplitude defect associated with them are each separated by only one cell from the nearest other pair.

Returning now to the case $\overline{G}=0.35$, the discussion of which was started with Fig. 16, we observe that even a flow of $f=1.0$ is sufficient to change a state that would otherwise be mostly steady (with some dynamics only in the vicinity of a few defects) into one that oscillates. In smaller systems, oscillations appear even at $f=0.1$. They seem to be impeded by disorder of the system, which perturbs the phase relations between neighboring oscillating cells. Therefore, they will more easily appear in small systems, which order completely as long as they are below the typical size of dynamical grains. Because for small flows order increases with increasing flow, the flow promotes oscillations. An oscillatory structure in turn can get rid of its topological defects more easily than a basically stationary one, as was demonstrated in Fig. 6 of I.

The scenario of the case $\overline{G}=0.6$ essentially repeats with the sole difference that the basic hexagonal pattern is now time dependent. A perfectly synchronized structure would be quasiperiodic in general, since the oscillation frequency of the $2\pi/3$ oscillations is unrelated to the drift velocity, imposing a second oscillation on each interface point with fixed x coordinate as it is passed by the traveling pattern. For $\overline{G}=0.35$, the transition to turbulent stripe patterns takes place at a larger f value than for bigger $\overline{G}$. It is located near $f=9.0$.

Finally, at $\overline{G}=0.25$, we have so far seen one case, in which disorder was completely eliminated by the flow, at $f=6.0$. The final structure is an ordered array of nonoscillating hexagons drifting at constant velocity. Ordering took place relatively fast, being complete at $t=500$. Patterns at zero flow and for flow values up to $f=4.0$ seem to be chaotic in time, with spatial disorder decreasing as the flow increases. This can be seen by a comparison of Figs. 21 and 22.

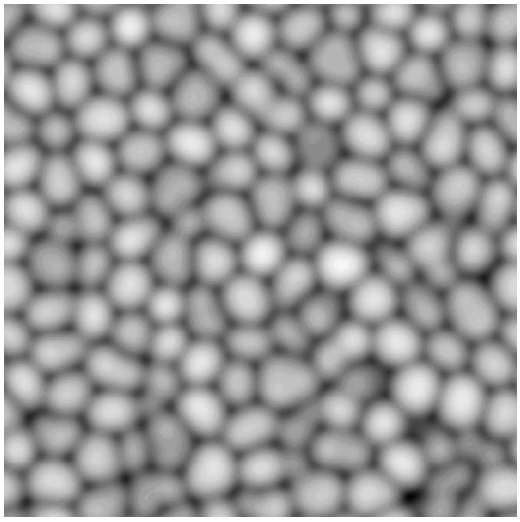

FIG. 21. Pattern at $\overline{G}=0.25$, $f=0.0$, system size 76.8×76.8 (grid spacing $h=0.3$), $t=1500.0$.

It is quite obvious, that the structure in Fig. 22 is much more ordered than that in Fig. 21, where no flow is present. Moreover, an oscillatory pattern can be made out that extends across most of the system.

Flows beyond $f=6.0$ have not yet been studied for $\overline{G}\leqslant0.25$. A more detailed investigation of these morphologies at low $\overline{G}$, which we believe to be at least close to the borderline (in the direction of decreasing $\overline{G}$) of a transition to weak turbulence, is planned for the future.

IV. CONCLUSIONS

The generic morphologies and dynamics of this system are: (a) steady traveling waves taking the form of stripes at

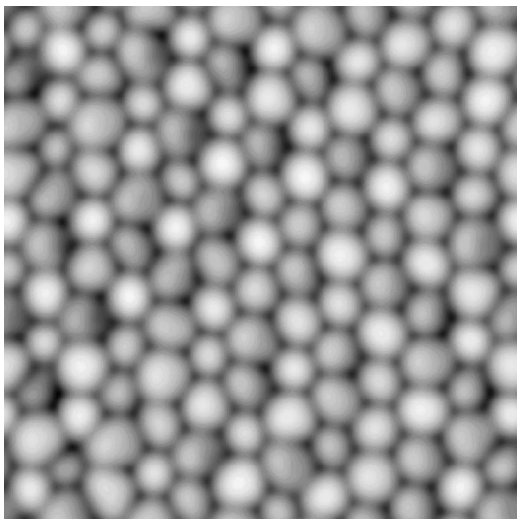

FIG. 22. Pattern at $\overline{G}=0.25$, $f=4.0$, system size 76.8×76.8, $t=1500.0$.

temperature gradients that would keep a planar front stable in the absence of flow — at a later stage these acquire a cellular modulation for small flows, (b) traveling hexagons when the Mullins-Sekerka instability becomes active, and (c) traveling hexagonal patterns with superimposed local oscillations, in which neighboring cells oscillate at a phase shift of $2\pi/3$. A variety of intermediate dynamic states arising from the competition between stripes and hexagons occur as well.

When the flow becomes large enough, it first changes the symmetry of the hexagonal pattern produced by the MS instability and eventually makes the cells disappear altogether. The emerging stripes start to undulate as the flow is increased further and finally become turbulent.

To observe the latter scenario in experiments, the distance ϵ to the absolute stability threshold has to be made small, considering the fact that typical Schmidt numbers of either transparent organic alloys (≈ 20) or metals (≈ 100) are rather large. To obtain a flow strength $f=1$ at $\epsilon=\frac{1}{10}$, the flow speed has to be on the order of the pulling velocity. Moreover, to reach the flow-induced destruction of hexagonal patterns at $\overline{G}<\frac{2}{3}$ this would have to be exceeded by at least a factor of five. In the case of liquid crystals where one can approach the limit of absolute stability arbitrarily closely, this should not present an unsurmountable obstacle. It must be kept in mind, however, that the asymptotic analysis leading to Eq. (1) assumes that the Schmidt number scales as $1/\epsilon$. Thus, it should become invalid when $1/\epsilon$ exceeds the Schmidt number by much.

Nevertheless, the appearance of flow-induced stripes *above* the critical value of $\overline{G}$ for the MS instability should be observable, even inevitable, if the critical value is approached slowly enough. This is due to the fact that the flow acts destabilizing in the conditions discussed here. ''Pure'' stripes will only be temporary at small flows, due to the transcritical nature of the bifurcation to hexagons, enabling a final transition to hexagonally modulated stripe patterns. Since this transition appears after a long time only (on the order of 1000 rescaled diffusion times), the preceding stripe dynamics should nonetheless remain observable.

Of course, in a real system, drifting patterns are restricted in their motion by boundaries. Therefore, the lateral motion described here would be possible only as a localized phenomenon. This suggests to investigate the same system numerically with boundary conditions that are not periodic, even though it is a bit difficult to imagine how a constant shear flow could persist in such a system. On the other hand, an attempt at an experimental realization of the periodicity of boundary conditions in the all important x direction would definitely be valuable. To this end, the solidification experiment would have to be performed in an annular container similar to the type used to impose a shear flow in the investigation of sand ripples [21]. Clearly, it is a considerable experimental challenge to combine this rotational motion — in a way that keeps the far-field flow constant — with the pulling of the sample in a temperature gradient.

Finally, we may conclude that the *characterization* of a pattern in terms of the defects of its amplitude is not as general as appeared at first sight. Although it allows both the description of stripe and hexagonal patterns (as opposed to the Voronoi defects, which are known to be useful only for the latter structures), it requires the *global* dominance of certain orientations. An amplitude equation description that preserves the rotational invariance of the basic equations [22] might extend the utility of the definition of defects or disorder [23], but it seems nontrivial to extract the corresponding amplitude from an arbitrary pattern, i.e., to develop the analog of complex demodulation. Therefore, at present the best way to distinguish between very different patterns and to quantify their difference seems to be via the Euler characteristic, for which there is, however, no known equation of motion.

ACKNOWLEDGMENTS

This work was supported by a PROCOPE grant for travel exchanges by the DAAD (German academic exchange service), Grant No. 9822777, and the Egide (corresponding French organization), Grant No. 01258ZD.

[1] Y. Marietti, J.-M. Debierre, K. Kassner, and T. Bock, preceding paper, Phys. Rev. E **63**, 066301 (2001).
[2] W.W. Mullins and R.F. Sekerka, J. Appl. Phys. **325**, 444 (1964).
[3] K.A. Jackson and J.D. Hunt, Met. Trans. AIME **236**, 1129 (1966).
[4] K. Kassner and C. Misbah, Phys. Rev. A **44**, 6513 (1991); **44**, 6533 (1991).
[5] A.K. Hobbs and P. Metzener, J. Cryst. Growth **118**, 319 (1992).
[6] K. Kassner, A.K. Hobbs, and P. Metzener, Physica D **93**, 23 (1996).
[7] N. Noël, Ph.D. thesis, Université d'Aix-Marseille III, 1996 (unpublished); N. Noël, H. Jamgotchian, and B. Billia, J. Cryst. Growth **181**, 117 (1997).
[8] N. Noël, H. Jamgotchian, and B. Billia, J. Cryst. Growth **187**, 516 (1998).
[9] K. Kassner, J.-M. Debierre, B. Billia, N. Noël, and H. Jamgotchian, Phys. Rev. E **57**, 2849 (1998).
[10] B. Billia, H. Jamgotchian, and H. Nguyen Thi, Metall. Trans. **22A**, 3041 (1991).
[11] K.R. Mecke, Phys. Rev. E **53**, 4794 (1996).
[12] H. Hadwiger, *Vorlesungen über Inhalt, Oberfläche und Isoperimetrie* (Springer, Heidelberg, 1957).
[13] Note that the Euler characteristic remains well defined in a system with periodic boundary conditions, even if we are not able to tell which color should be assigned to the background. It is just formula (5) that will not work anymore in this case (due to the toroidal topology).
[14] S. Rasenat, V. Steinberg, I. Rehberg, Phys. Rev. A **42**, 5998 (1990).
[15] Y. Marietti, Ph.D. thesis, Université d'Aix-Marseille III, 2000 (unpublished).
[16] S. Kai and K. Hirakawa, Suppl. Prog. Theor. Phys. **64**, 212 (1978).

[17] A. Joets and R. Ribotta, Phys. Rev. Lett. **60**, 2164 (1988).
[18] I. Rehberg, S. Rasenat, J. Fineberg, M. de la Torre Juárez, and V. Steinberg, Phys. Rev. Lett. **61**, 2449 (1988).
[19] I. Rehberg, S. Rasenat, and V. Steinberg, Phys. Rev. Lett. **62**, 756 (1989).
[20] M. Dennin, M. Treiber, L. Kramer, G. Ahlers, and D. S. Cannell, Phys. Rev. Lett. **76**, 319 (1996).
[21] A. Betat, V. Frette, and I. Rehberg, Phys. Rev. Lett. **83**, 88 (1999).
[22] G.H. Gunaratne, Q. Ouyang, and H.L. Swinney, Phys. Rev. E **50**, 2802 (1994).
[23] G.H. Gunaratne, R.E. Jones, Q. Ouyang, and H.L. Swinney, Phys. Rev. Lett. **75**, 3281 (1995).